Competitive enhancement of CO_2 reduction reactions versus hydrogen evolution for high surface area electrodes: a comparative study for Cu and Ag nanomesh

Nina Plankensteiner[a,b,c,*], *Noah Rondou*[a,b,c] *Martijn J.W. Blom*[a,c], *Anna Staerz*[a,b,c], *Cole Smith*[a,c], *Maarten Mees*[a,c], *Philippe M. Vereecken*[a,b,c*]

[a] imec, Kapeldreef 75, 3001 Leuven, Belgium

[b] KU Leuven, M^2S, cMACS, Celestijnenlaan 200F, 3001 Leuven, Belgium

[c] EnergyVille-Thor Park 8310, 3600 Genk, Belgium

KEYWORDS: Electrocatalysis, carbon dioxide reduction, nanostructured electrodes, CO_2 mass transport, (bi)carbonate equilibria

*Corresponding authors: nina.plankensteiner@imec.be, philippe.vereecken@imec.be

ABSTRACT

High surface area electrodes are an attractive option for electrocatalytic CO_2 reduction reaction (CO_2RR) on the pathway towards commercialization of this compelling technology. The intrinsic large quantity of catalytic surface sites opens the potential for high currents per geometric electrode area at low overpotentials, if mass transport can be ensured. However, CO_2RR from aqueous solutions is limited by the solubility of ~0.034M CO_2 in water at 1 bar of CO_2 partial pressure. In this work we studied electrochemical CO_2RR on 3µm thin Cu and Ag nanomesh electrodes with ~40-50x enhanced surface area compared to planar electrodes in aqueous bicarbonate solutions. The regular 3D-nanowire networks or nanomeshes were fabricated by metal plating in 3D nanoporous anodized aluminum oxide templates The obtained partial currents for hydrogen evolution reaction (HER) and CO_2RR matched very well with that modelled by mass transport including the active CO_2 depletion by carbonate equilibria in the alkalinized diffusion layer, limiting the maximum (diffusion limited) partial current density for pure CO_2RR to 9mA/cm^2. Interestingly, it was found that the high surface area of the nanomesh electrodes primarily promoted the more catalytic reaction, i.e., with the lowest overpotential. On the Cu nanomesh the HER was preferentially enhanced with a reduction in overpotential of ~450mV, moving the potential even outside the window of some of the CO_2RR products found at planar electrodes. On the Ag nanomesh, on the other hand, the CO_2RR to CO was preferred over HER where the 250mV lowering of the overpotential for the same current density results in an increased energy efficiency for CO_2RR. These findings highlight the need to investigate whether the desired CO_2RR or the competing HER will be enhanced by high surface area electrodes in relation to the nano-architecture and the catalysts nature as an important step forward towards upscaling the CO_2RR electrolysis technology.

GRAPHICAL ABSTRACT

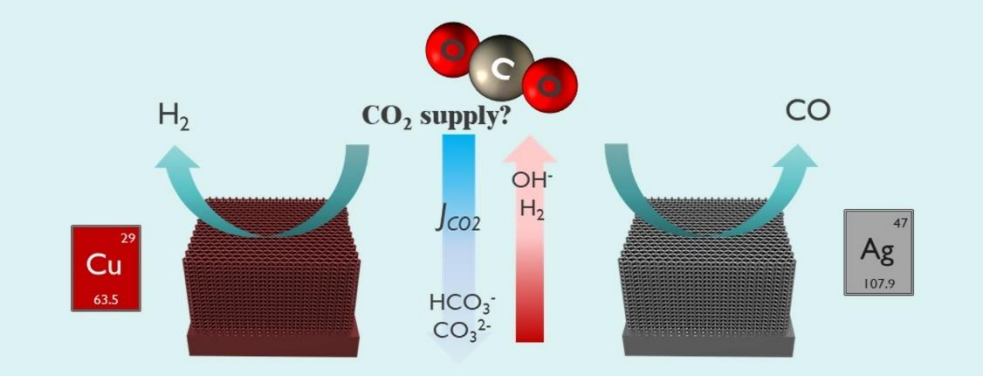

1. Introduction

Electrocatalytic CO_2 reduction reaction (CO_2RR) is an attractive approach to mitigate CO_2 emissions and concurrently offers together with electricity from renewable sources a carbon-neutral feedstock of chemicals for industry and as fuels. Since the pioneering work by Hori et al. in the 1980s[1] a lot of progress was reported in this field and the electrocatalytic CO_2RR is currently a highly active area of research with several hundreds of papers published every year.

Nonetheless, in order to make this technology viable further improvement in throughput, operation at high current densities >200mA/cm^2 and low overpotentials, excellent selectivity towards the desired CO_2RR product and longer operation lifetime are the key obstacles to overcome.[2]To tackle some of these challenges nanostructured electrodes of copper or silver are especially attractive.[3] Nanostructured catalysts offer several advantages over their planar counterparts. Firstly, due to their high electrochemical active surface area (ECSA) a high current densities per geometric electrode surface area can be achieved[4,5] thus, lower overpotentials for

the CO_2RR need to be applied making the reaction economically more attractive. This was first demonstrated on oxide-derived nanostructured copper electrodes that required a 500mV lower overpotential for the reaction to C_1 products (CO and HCOOH) compared to planar electrodes.[6] Secondly, it has been found that modified electrocatalytic properties and confinement in the micro/mesoporous structure may result in different reaction pathways and possibly higher selectivity towards the highly desired formation of C_{2+} or even C_{3+} products e.g. in Cu nanocavities[7], regular-ordered mesoporous Cu[8] or Cu nanocrystal cubes[9,10] that resulted in the formation of propanol or high selectivity towards C_2 products. Thirdly, high surface area electrodes show higher stability since they are less prone to extrinsic poisoning effects, such as electrode deactivation by metal impurities.[11,12]

When studying catalytic activity and reaction kinetics of nanostructured high surface area electrodes towards CO_2 reduction aqueous electrochemical cells are commonly used.[13] In such cells, the low solubility (34mM at 1 bar and 25°C)[14] and slow diffusion of CO_2 ($1.9*10^{-5}$ cm^2/s at 25°C)[15] next to the active CO_2 self-depletion are the cause of large CO_2 concentration gradients and low CO_2 concentration near the cathode surface, limiting the CO_2RR to a maximum current density of ~$35mA/cm^2$.[13] The here introduced concept of "active CO_2 self-depletion" is used to describe the decreased availability of CO_2 at the electrode due to the electrocatalytic CO_2R reactions and solution buffer equilibria converting CO_2 to (bi)carbonate. At the same time the alkaline hydrogen evolution reaction (HER) with similar overpotentials as the CO_2RR is largely not affected by mass-transport limitations and especially at high current density with limiting CO_2 mass-transport large amounts of H_2 instead of CO_2RR products are formed.[5,16] This behavior is especially pronounced at high surface area electrodes since the high current densities per geometric catalyst area introduces rapid CO_2 depletion, thus, for such

catalysts it is especially critical to deduce mass transport limitations from the catalyst activity towards CO_2RR.

In this article we discuss the CO_2 reduction reaction on high surface area regular-ordered Cu and Ag 3D-nanowire-networks as electrodes in an aqueous potassium bicarbonate electrolyte. These so-called nanomesh electrodes are fabricated by electrochemical plating of the corresponding metal catalyst in a 3D-porous aluminum oxide (AAO) template. Their attractive combination of high porosity (76%) and high volumetric surface area of 26cm^3/cm^2 for electrocatalysis was already demonstrated for water electrolysis using nickel nanomesh electrodes.[17,18] Here, Ag and Cu nanomesh electrodes (with ~40-50x enhanced surface area compared to planar electrodes see measurements SI) were fabricated by electroplating in the AAO template and characterized towards the CO_2RR in an aqueous electrochemical H-type cell. While Cu has the unique ability to convert CO_2 to valuable multi-carbon products such as ethylene (C_2H_4) or alcohols (methanol, ethanol or even beyond)[4] but struggles with the competition between the hydrogen evolution reaction (HER)[19,20], Ag is one of the most active catalysts that selectively convert CO_2 to CO[19,21,22] which is in the form of syngas (mixed with H_2) an important precursor for the chemical industry. The catalytic differences for CO_2RR on single metal catalysts is commonly explained by the binding energy of CO* as key reaction intermediate.[23,24] While Ag binds CO* weakly and easily releases CO as its main CO_2RR product, Cu possesses an intermediate binding strength for CO* which is thought to be critical in the formation of the C-C bond to higher carbon products such as C_2H_4 with larger overpotentials needed.[1,25] At the same time H* adsorbs more strongly on Cu than Ag promoting the HER on Cu which limits the faradaic efficiency in forming CO_2RR products.[19,24]

The versatile nanomesh fabrication approach here allows the comparison between two metal electrodes with different catalytic properties towards the CO_2RR with same nano-architecture and similar high surface area. The choice of Cu and Ag enables to investigate in particular the competition of CO_2RR and HER in these nanostructures and the enhancement of specific reaction pathways by the high surface area electrodes. At the same time mass transport limitations due to active CO_2 depletion in the nanomesh electrodes will be examined. This work highlights the need to understand the interplay between mass transport and catalytic properties on high surface area electrodes in order to tune them towards the enhancement of the desired CO_2RR reaction pathway.

2. Experimental

2.1. Fabrication of Cu and Ag Nanomesh electrodes

Cu and Ag nanomesh electrodes were obtained by plating in 3D-porous aluminum oxide (AAO) templates. The AAO template was formed by anodization at 40V in 0.3M oxalic acid in the same cell setup and under the same experimental conditions as previously described.[17] In short, a glass cell with an extra reference electrode compartment is clamped on the wafer substrate placed on a temperature controller (at 30℃) whereas a silicone O-ring exposes the anodization area of 23.74cm^2. The constant anodization voltage was controlled with an Autolab PGSTAT100 potentiostat/galvanostat and a titanium gauze (60 mesh, Alfa Aesar, 46828) was used as counter electrode.

To fabricate the Cu nanomesh, Cu was plated in the AAO template on the Si/TiN wafer substrate under galvanostatic conditions at -30mA/cm2 at 30℃ (based on the actual deposition area given by the AAO porosity of 24%) until the total charge passed reached a value of 1.8 C/cm^2_{geo} (in respect to the geometric surface area). The freshly prepared Cu plating solution contained 0.5M copper sulphate pentahydrate ($CuSO_4 \cdot 5H2O$, Sigma Aldrich 209198) and 0.25M sulphuric acid (H_2SO_4 96%, Sigma Aldrich, 258105). As counter electrode a copper sheet (Sigma Aldrich, 349151) and an Ag/AgCl reference electrode (BASi RE-5B 3M KCl) were used. Finally, the AAO template was removed by a 30min immersion in 0.5M KOH at room temperature. Using these parameters, a 3.4µm thick Cu nanomesh attached to the Si/TiN wafer substrate was obtained (see **Figure 1**).

The Ag nanomesh was prepared in a similar manner using a freshly prepared Ag-thiosulfate bath for plating in the AAO template. The bath was prepared as follows: Firstly, a clear silver nitrate solution was prepared by dissolving 6g of $AgNO_3$ (Sigma Aldrich 209139) in 50ml of DI water under magnetic stirring. A second solution of 6g sodium metabisulfite ($Na_2O_5S_2$, Sigma Aldrich S9000) dissolved in 50ml DI water was added to the $AgNO_3$ solution to form a white precipitate. Lastly, 60g of sodium thiosulfate ($Na_2O_3S_2$, Sigma Aldrich 217263) dissolved in 100ml DI water was added to the $AgNO_3$ solution to form the silver thiosulfate complex resulting in a slightly yellow, clear plating solution of pH=5.4 with a total volume of 200ml. The final solution concentrations were 0.22M AgNO3, 1.90M $Na_2O_3S_2$ and 0.16M of $Na_2O_5S_2$. Ag was deposited in the AAO at room temperature (20℃) under galvanostatic conditions with a short pulse at -10mA/cm^2_{geo} of 2s and then at -2mA/cm^2_{geo} for 800s (based on actual deposition area in AAO) till a charge of 1.6 C/cm^2_{geo} passed. A titanium gauze (60 mesh, Alfa Aesar, 46828) and an Ag/AgCl counter and reference electrode were used. The template was removed with the same

procedure as described for the Cu nanomesh and the resulting Ag nanomesh on the Si wafer was 3.2µm thick (see **Figure 1**).

2.2. Planar Cu and Ag electrodes

Planar Cu electrodes were prepared by plating Cu from the same solution and using the same glass cell as used for the Cu nanomesh fabrication. As substrate a Si/TiW(30nm)/Cu(150nm) was used and a 1.4µm Cu layer was obtained after a charge of 3.75C/cm^2_{geo} passed using galvanostatic deposition at -15mA/cm^2. Reference and counter electrode were a Cu foil and Ag/AgCl respectively. Ag electrodes were prepared by thermal evaporation of 100nm Ag on Si/TiW(30nm)/Cu(150nm) substrates using an Alcatel thermal e-beam evaporator.

2.3. Characterization of nanomesh and planar electrodes

The cross-section morphology of Ag and Cu nanomesh electrodes were characterized by a Nova 200 scanning electron microscope (SEM) at 7 kV with a through the lens detector (TLD) and is shown in **Figure 1**. The electrochemical active surface area was determined by double-layer capacitance measurements (see SI).

2.4. Electrocatalytic CO_2RR in liquid H-type cell

2.4.1. H-cell configuration and experimental conditions

The electrocatalytic CO_2RR experiments were carried out in an air-tight H-type Teflon cell, in which a commercial anion-exchange membrane (Fumasep FAA PK-130) separated the anolyte

and catholyte chamber (see cell schematic in SI). An Ag/AgCl (3M KCl, redox.me) reference electrode was immersed in the catholyte close to the cathode surface. A Si wafer coated with SiO_2(300nm)/TiO_2(10nm)/Pt(60nm) was used as anode. Both electrode areas, 2cm^2 for the cathode and 4.75cm^2 for the anode were defined using a Teflon gasket. All the measured potentials are reported against the reversible hydrogen electrode (RHE) calculated from $U_{RHE} = U_{Ag/AgCl} + 0.21V + 0.0592V * pH$ (0.2M KHCO3 pH = 7.25), whereas the bulk solution pH was measured with a Metrohm pH lab connected to pH probe (Primatrode 6.0228.010).

For each CO_2 reduction experiment a constant current density (in respect to the geometric exposed cathode area of 2cm^2) was applied for 100min using a Biologic VSP potentiostat with integrated impedance module. Prior to this, electrochemical impedance spectroscopy (EIS) at open circuit potential, frequencies 100mHz-10kHz and amplitude 20mV, was measured to determine the uncompensated solution resistance for the manual iR correction of the recorded potentials. Each experiment was done using a fresh cathode, while the Pt anode was rinsed with DI water and re-used for all experiments. The electrolyte, 0.2M potassium bicarbonate ($KHCO_3$, Sigma Aldrich, 237205) was purged for 30min with CO_2 prior to the electrolysis experiments. The purity of the electrolyte before and after electrolysis was measured with ICP-OES. While Ni and Cu concentrations were below the detection limits of 5 and 4ppb, negligible amounts of Zn (15ppb) and Fe (11ppb) were measured in the initial electrolyte. The catholyte and anolyte chamber were each filled with 15ml of CO_2-purged $KHCO_3$ resulting in a 3mL gas headspace. The cell was placed on a Metrohm 728 stirrer to rotate the 1cm stirring bar in the cathode chamber for electrolyte mixing and gas bubble removal from the electrode surface. A continuous CO_2 gas flow of 7.5ml/min purged at the cell bottom via a porous glass frit (VitraPOR with 10-

16µm porosity, Robu Glasfilter Geräte) ensured continuous CO_2-saturation in the electrolyte[26] and eluted gaseous products into the online gas chromatograph (GC).

2.4.2. Liquid and gaseous product quantification during CO2 reduction:

The GC (customized ThermoFisher Trace 1300 from Interscience Netherlands) was equipped with two channels. Channel 1 was used to detect CO, CH_4 and C_{2+} hydrocarbons such as C_2H_4 with a flame ionization detector (FID) connected to a methanizer using He as the carrier gas. H_2 is detected on Channel 2 with a thermal conductivity detector (TCD) and using N_2 as the carrier gas. Component separation was done using several micropacked ShinCarbon columns (SC-ST 100-120 0.5m*1/16" SS) and to separate C_2H_4 and alcohols a fused silica column (Rtx-624 3µm 30m*0.53mm) was used. The GC was calibrated using Standard gas mixtures in several concentrations between 10 and 1000ppm in N_2 as balance gas (Nippon gas). The in-line gas injection sequence directly from the electrochemical outlet flow was controlled via Chromeleon software (ThermoFisher). Liquid catholyte and anolyte were analyzed after the constant current step of 100min via manual injection of a 1µl sample volume in an SSL-port.

The faradaic efficiency and partial current densities of CO_2RR products were calculated based on the average of several gas samples collected every 10min during 10-60min of the constant current density applied. During this sampling period the deviation in the measured potential only showed minor deviations arising from the gas flow and stirring of the electrolyte (see also SI). Faradaic efficiency is defined as the fraction of current (or charge) utilized to produce the CO_2RR product according to **equation 2.1** whereas the ppm of product detected by the GC was directly inserted:

$$FE = \frac{j_{product}}{j_{total}} = \frac{ppm_{product} \cdot 10^{-6} \cdot \frac{p\phi_v}{RT} \cdot zF}{j_{total}} \quad (2.1)$$

The amount of moles in the sample volume was calculated from the ideal gas equation, in which p is the pressure (1.013 bar), ϕ_v the gas flow rate (m^3/s), R the gas constant (8.314 J/K*mol), T the temperature (298.15 K), z the number of electron transferred, F the Faraday constant (96485 sA/mol) and j the partial and total current density. For the gas flow the actual CO_2+products outlet flow was measured directly from the back of the GC outlet since the products were constantly transported through the equipment (Restek ProFLOW 6000 Flowmeter).

2.5. Computational modelling of CO_2 mass transport limitations

A steady-state film diffusion model was implemented in a similar fashion as described by Gupta et al.[27] In the film diffusion model depletion and accumulation of species is localized near the electrode in a (hypothetical) stagnant liquid layer with thickness δ where mass transport is assumed to occur solely by diffusion. The thickness of the film corresponds to the diffusion layer as commonly referred to in electrochemistry. Even though, bubble formation and (electro)-migration of charged species may influence mass transport at high current densities, they are not considered here as only moderate current densities are modeled. Outside of this diffusion layer the bulk solution is assumed to be perfectly mixed resulting in flat bulk concentration profiles. The relevant dissolved species incorporated in the model are: CO_2, HCO_3^-, CO_3^{2-} OH^- and H^+. Due to the low fraction of carbonic acid in aqueous solutions this species is not considered in the model. The CO_2 to bicarbonate reaction (4.3) is known to be a reaction with a small rate constant whilst the other acid-base reactions can be assumed at equilibrium.[27] For the CO_2RR only the CO product is considered, which is an appropriate approximation for Ag electrodes.[1,27] At the

electrode boundary the flux (J_n) of hydroxide and CO_2 are explicitly defined based on the partial current density (j_n) for CO_2RR and HER as per equation 2.5.1 and 2.5.2.

$$J_{CO_2}(x = 0) = \frac{-j_{CO_2RR}}{2F} \tag{2.5.1}$$

$$J_{OH^-}(x = 0) = \frac{j_{CO_2RR}}{F} + \frac{j_{HER}}{F} = \frac{j_{total}}{F} \tag{2.5.2}$$

This means that mass transport is described independent of electrocatalytic properties, making the results generally applicable for CO_2RR that produces mainly H_2 and CO. The bicarbonate and carbonate species are considered to not be electrochemically active as per literature[27] and thus, the flux of these species at the electrode surface is taken to be 0. The diffusion coefficients, equilibrium constants and rate constant for (bi)carbonate formation were obtained from literature and are given in the SI. The equations as listed in the SI with the corresponding symbols and units were solved utilizing COMSOL Multiphysics 6.1.

3. Results

3.1. CO_2RR products and partial current densities on Cu electrodes

The electrochemical CO_2RR on Cu electrodes was measured in a CO_2-purged potassium bicarbonate (0.2M $KHCO_3$) electrolyte by applying constant current steps per geometric electrode area for >1h (see current transients in supporting info). **Figure 2** and **Table 1** depict the partial current densities ($j_{partial}$) and faradaic efficiencies (FE) toward gaseous CO_2RR products and H_2 from the HER on planar Cu and nanomesh electrodes. The shown values are calculated

from the average of several in-situ product samples during a period of stable electrochemical potential (10-60min of the experiment) with constant current density applied (5 up to 25mA/cm^2) from the CO_2+product stream by gas chromatography. On planar Cu at all current densities significant amounts of CH_4 and C_2H_4 up to 40% faradaic efficiency and small amounts CO are detected. These products are mostly absent during CO_2RR on the Cu nanomesh which instead dominantly makes H_2. On the Cu nanomesh only minor amounts of CO and C_2H_4 are detected with maximum partial current densities of 0.41mA/cm^2 (-0.75V vs RHE) and 0.66mA/cm^2 (-0.93V vs RHE) respectively. Note, the total faradaic efficiencies deviate from 100%, which was attributed to the standard deviation between the measurements, the possible formation of formate below the GC detection limit as well as minor quantification of alcohols (mostly methanol and ethanol) with ~1% faradaic efficiency. A comparison of faradaic efficiency normalized to 100% is shown in the SI. The maximum partial current density towards CH_4 and C_2H_4 on planar Cu is 3.8 mA/cm^2 (-1.19V vs RHE) and 2.45 mA/cm^2 (-1.27V vs RHE) respectively.

Table 1 Partial current densities and iR-corrected potentials on Cu electrodes including the standard deviation calculated from several GC samples as described in section 2.4.2.

Current density applied j_{total} (mA/cm^2)	iR-corr. Potential (V) vs RHE	Partial current densities to CO2RR products (mA/cm^2)			
		H_2	CO	CH_4	C_2H_4
Cu planar					
5	-0.94	1.64 +/- 0.18	0.14 +/- 0.06	1.03 +/- 0.04	0.91 +/- 0.09
10	-1.13	7.45 +/- 0.51	0.23 +/- 0.03	1.36 +/- 0.95	0.70 +/- 0.01
15	-1.19	9.06 +/- 0.03	0.11 +/- 0.01	**3.84** +/- 0.31	2.30 +/- 0.14
25	-1.27	19.79 +/- 3.41	0.05 +/- 0.01	3.51 +/- 0.37	**2.45** +/- 0.01
Cu Nanomesh					
5	-0.50	4.03 +/- 0.02	0.10 +/- 0.03	0.02 +/- 0.00	0.21 +/- 0.01
10	-0.57	8.98 +/- 0.17	0.17 +/- 0.02	0.13 +/- 0.01	0.23 +/- 0.04
15	-0.75	12.93 +/- 0.83	0.41 +/- 0.02	0.05 +/- 0.01	0.54 +/- 0.02
25	-0.93	22.27 +/- 0.67	0.41 +/- 0.01	0.05 +/- 0.00	0.66 +/- 0.08

Compared to planar Cu, on the nanomesh 400-500mV lower overpotentials are observed for the same current densities per geometric electrode area applied. This observation can be attributed to the high surface area of the nanomesh electrodes (~52x higher area, see measurements supporting information). To reach the required potential for the formation of C_2H_4 and CH_4 as seen on planar Cu, a ~5x higher current density would be required. At these high current densities CO_2 mass transport will play an essential role in limiting the formation of CO_2RR products, while the HER can still proceed without significant transport limitations. Further, it was shown in literature that the CO_2RR reaction pathways to C_2H_4 and CH_4 on Cu are pH dependent.[28,29] The pH profile in the diffusion layer and at the electrode surface will be further addressed in the discussion below.

3.2.CO_2RR products and partial current densities Ag electrodes

The CO_2RR on Ag electrodes was measured analogously to Cu using the same applied constant current densities per geometric electrode area (current transients in supporting info). **Figure 3** and **Table 2** show the partial current densities and faradaic efficiencies to gaseous CO_2RR products and H_2 on planar Ag and nanomesh electrodes. On both electrodes the major products are CO and H_2. On planar Ag, there are additionally minor amounts of CH_4 and C_2H_4 detected with partial current densities <1mA/cm^2 (see **Table 2**). On both Ag electrodes a minor amount of ethanol with <2% FE was detected. The deviation from 100% FE can be attributed to the reasons mentioned above and normalized values are shown in the SI. The maximum achievable partial current density towards CO on both electrodes is similar 6mA/cm^2 (nanomesh) and 5.6mA/cm^2 (planar). However, the electrode potential at the maximum current density towards CO is 250mV

lower on the nanomesh compared to planar Ag. The pronounced decrease in overpotential is attributed to the high surface area of the nanomesh electrode ~43x higher than planar electrodes (see surface area measurements in supporting info). Since similar maximum partial current densities to CO are observed on both electrodes, CO_2 diffusion limitation at the electrode surface most likely play a dominant role. This will be further examined in **section 4.1**.

Table 2 Partial current densities and iR-corrected potentials on Ag electrodes including the standard deviation calculated from several GC samples as described in section 2.4.2.

Current density applied j_{total} (mA/cm^2)	iR-corr. Potential (V) vs RHE	Partial current densities to CO_2RR products (mA/cm^2)			
		H_2	CO	CH_4	C_2H_4
Ag planar					
5	-1.1	0.84 +/- 0.017	2.87 +/- 0.31	0.02+/- 0.01	0.10 +/- 0.10
10	**-1.3**	4.04 +/- 0.38	**5.58** +/- 0.18	0.39 +/- 0.13	0.23 +/- 0.31
15	-1.41	11.61 +/- 1.33	3.89 +/- 0.47	0.85 +/- 0.43	0.48 +/- 0.48
25	-1.47	21.28 +/- 1.24	2.27 +/- 0.40	0.18 +/- 0.02	0.13 +/- 0.13
Ag Nanomesh					
5	-0.84	0.44 +/- 0.02	3.63 +/- 0.37	0.04 +/- 0.01	0.09 +/- 0.03
10	**-1.05**	2.74 +/- 0.52	**5.96** +/- 1.24	0.06 +/- 0.01	0.11 +/- 0.04
15	-1.18	9.32 +/- 0.29	4.73 +/- 0.02	0.04 +/- 0.00	0.06 +/- 0.00
25	-1.36	20.26 +/- 1.62	3.12 +/- 0.27	0.01 +/- 0.00	**0.01** +/- 0.00

4. Discussion

4.1. CO_2 mass transport effects limiting the CO_2RR current density

In this discussion the main factors limiting the mass transport of CO_2 to the high surface area electrodes are determined. As mentioned earlier, the CO_2RR in typical aqueous electrochemical H-type cells is highly susceptible to the CO_2 concentration gradients near the electrode surface. The limited solubility of CO_2 in aqueous solutions results in low bulk concentration of around 34mM at 1 bar of CO_2 partial pressure (25°C).[14] The magnitude of the CO_2 concentration gradient depends on convective mixing during operation. Solution agitation through continuous CO_2 purging in the cell, electrolyte circulation or stirring have significant influence on the CO_2 supply to the electrode. First, the steady state diffusion layer thickness is characterized to determine the maximum CO_2 flux towards the electrode surface under cell operation. Secondly, the role of active CO_2 depletion due to CO_2RR and the conversion to (bi)carbonate due to alkalinization by produced OH^- according to the (bi)carbonate equilibrium is discussed by means of the simple model reaction of CO_2 to CO.

4.1.1. CO_2 flux to electrode surface under steady state cell operation conditions

The limiting current density towards CO_2 reduction products on planar electrodes can be estimated by the incoming CO_2 flux through the diffusion layer according to the film diffusion model:

$$j_{lim,CO_2} = nFD_{CO2}C_{0,CO2}/\delta \qquad (4.1)$$

Where, n is the number of electrons transferred in the electrochemical reaction, F the Faraday constant (96485 $C.mol^{-1}$), D_{CO2} the diffusion coefficient of CO_2 ($1.91*10^{-9}$ $m^2.s^{-1}$ in water at infinite dilution)[15] and $C_{0,CO2}$ the bulk concentration (34 mM)[14] of CO_2 in the electrolyte. The thickness of the diffusion layer δ determines the limiting current density (j_{lim}) according to equation (4.1). The limiting current for CO_2 electroreduction to CO, CH_4 and C_2H_4 is plotted in **Figure 4** as a function of δ. The diffusion layer in aqueous H-type cells with a stagnant electrolyte is typically ~100µm,[1,16,27] which limits the current density in this initial assessment for all three products mentioned above to ~50mA/cm^2. To form CO_2RR products with current densities >200mA/cm^2 as required for the practical implementation of this technology, much smaller diffusion layer thicknesses (<25µm) are needed. This can be achieved with high liquid flow rates such as on a rotating disk electrode or by limiting the liquid layer thickness as in a gas diffusion electrode.

In the cell used in this work, CO_2 was supplied at a constant flow rate to the electrolyte at the bottom of the catholyte chamber through a porous glass frit. A small magnetic stirring bar was placed on the bottom of catholyte chamber to ensure mixing and removal of gas bubbles from the cathode and the Teflon gasket (see SI). To assess the effect of magnetic solution stirring and CO_2 purging on the diffusion layer thickness, the diffusion limited current (j_{lim}) of the oxygen reduction reaction (ORR) for an O_2-saturated 0.5M H_2SO_4 solution was determined, from which the diffusion layer thickness was determined (see SI). With and without electrolyte stirring the diffusion layer thicknesses were 110µm and 410µm respectively, hence, the agitation caused by stirring decreased the diffusion layer thickness by a factor 4. The diffusion coefficient of O_2 in 0.5M H_2SO_4 is with $1.8*10^{-9}$ m^2s^{-1} [30,31] almost identical to the one reported for CO_2 ($1.91*10^{-9}$ m^2s^{-1})[15] As per equation 4.1. the theoretical maximum current densities for formation of CO,

CH_4 and C_2H_4 are then 11.4, 45.4 and 34.1 mA/cm^2, respectively due to the increasing amounts of electrons transferred per CO_2 molecule (see also **Figure 4**). The partial currents found within this work on Cu and Ag electrodes were sufficiently lower than the calculated diffusion limited values. Hence, the CO_2 flux to the electrode is initially high enough to carry the current, however, other mass-transport related effects and catalyst activity may limit the CO_2 reduction kinetics. Also, these limiting current values do not yet reflect the consumption of CO_2 due to (bi)carbonate formation.

4.1.2. Active CO_2 self-depletion due to alkalinization and (bi)carbonate equilibrium

As discussed above, sufficient CO_2 is supplied to the electrode to theoretically enable higher partial current densities towards CO_2RR products than experimentally observed. This is explained by the fact that on top of the amount of CO_2 depleted by the CO_2RR, part of the CO_2 is consumed by its conversion to (bi)carbonates due to alkalinization. The effect on the limiting current density of CO_2 reduction including these reactions is investigated by a simple steady-state diffusion model based on the CO_2 conversion to CO and the (bi)carbonate equilibria reactions as shown below:

$$CO_2\ (aq) + H_2O + 2e^- \rightarrow CO\ (g) + 2OH^-\ (aq) \quad (4.2)$$

$$CO_2\ (aq) + OH^-\ (aq) \leftrightarrows HCO_3^-\ (aq) \quad (pK_1=6.37) \quad (4.3)$$

$$HCO_3^- + OH^- \leftrightarrows H_2O + CO_3^{2}\ (aq) \quad (pK_2=10.25) \quad (4.4)$$

The depletion and accumulation of species is assumed localized near the electrode in a theoretical stagnant liquid layer with determined thickness δ of 110µm (under cell operation)

where mass transport occurs solely by diffusion. In addition, the generation of OH^- ions and the resulting increased alkalinization, as a consequence of the CO_2RR to CO (see equation 4.2) and the HER as shown in equation (4.5) were included in the model:

$$2H_2O + 2e^- \rightarrow H_2\ (g) + 2\ OH^-\ (aq) \qquad (4.5)$$

The formed OH^- ions concurrently react with CO_2 according to formula (4.3) and (4.4) to form HCO_3^- and CO_3^{2-} and thereby actively reduce the CO_2 concentration at the electrode surface and in the adjacent diffusion layer as plotted for different current densities in **Figure 5(a)** based on the experimental determined CO:H_2 ratio on planar Ag inserted in the model (see Figure 3, Table 2). The maximum diffusion limited current density in absence of (bi)carbonate formation for 34mM of dissolved CO_2 *(aq)* at 1 bar partial pressure is 11.4mA/cm^2 at steady condition in our cell. According to the model accounting for the carbonaceous equilibrium, diffusion limitation of CO_2 supply (FE<100%) is reached at 9 mA/cm^2 (**Figure 5(c)** and **5(d)**). At an applied current density of 5mA/cm^2, the reaction is still under mixed control and the CO_2 surface concentration is about half the bulk concentration. However, instead of a linear concentration profile expected for mass transport limited supply of oxidant species, a bent profile is obtained due to the active CO_2 self-depletion from by reactions (4.3) and (4.4). At current densities beyond the diffusion limited current, the bending of the profiles continues as the OH^- concentration increases from reaction (4.5). Although this increases the CO_2 flux coming from bulk solution, it does not result in more CO_2 at the surface, it is converted to (bi)carbonate within the diffusion layer. The pH gradient throughout the diffusion layer (and also the nanomesh) from cathodic reactions (4.2) and (4.5) is shown in **Figure 5(b)**. The maximum achievable partial current density to CO as a function of the total geometric current density applied according to the model is plotted in **Figure 5(c)**. Below 9mA/cm^2 the CO_2 flux is sufficient to convert CO_2 completely to CO (FE

=100%). For current densities larger than 9mA/cm^2 the active self-depletion of CO_2 increases rapidly due to the hydrogen evolution reaction and alkalinization of the diffusion layer thereby decreasing the faradaic efficiency for CO which eventually reaches zero around 35mA/cm^2 (as shown in **Figure 5(d)).** Therefore, active self-depletion might explain why oftentimes a decrease in partial current density to CO_2RR is observed at high overpotentials: The limiting current density for CO_2RR decreases with total current density, meaning results can be inadvertently obtained under mass transport limited conditions.

The experimental results for planar Ag and nanomesh electrodes follow the trend of the modelled partial current density towards CO as a result of active self-depletion (**Figure 5(c and d)**). The highest amount of CO was experimentally observed at 10 mA/cm^2 which correlates well with the model. At this current density no significant active self-depletion is expected and catalyst reaction kinetics might explain the slight deviation from the model. Strikingly, at higher current densities of 25mA/cm^2 the measured partial current densities overlay very well with the modelled values for CO formation. Note, although CO_2 mass transport limitation due to rapid CO_2 consumption in the electrochemical reaction to CO and solution equilibria appears to be the major limiting factor >10mA/cm^2 in the data within this work, there are also other (mass transport) limitations that will impact the CO_2RR such as surface wetting properties or gas bubble transport.

Regarding the local pH at the electrode surface and in the diffusion layer due to production of OH^- ions during CO_2RR and especially HER at the planar Ag electrode (**Figure 5(b)).** Already at the lowest current density applied (5mA/cm^2), the electrode surface pH increases to ~9.5 from pH=7.25 of the bulk electrolyte. With increasing current density, the pH at the cathode increases up to >11.0 for an applied current density of 25mA/cm^2. These values are well in accordance

with the surface pH calculated by Gupta et al[27] at 5mA/cm^2 for a diffusion layer thickness of 100µm and other literature reports.[1,32–34] The high surface pH will have an additional effect on CO_2RR reaction pathways as discussed below for Ag and Cu electrodes. Throughout the nanomesh thickness, an additional diffusion gradient will exist which can affect the CO_2RR inside the nanomesh. However, as the nanomesh thickness of ~3µm is only a fraction of the diffusion layer thickness (~110µm), it will not affect the modelled concentration profiles of **Figure 5**. Note that this is in stark contrast with literature working with metal foam or alike electrode architectures where the diffusion layer thickness is typically less than the electrode thickness or in the same order of magnitude.[5,35–37]

4.2. CO_2RR on high surface area Ag and Cu Nanomesh electrodes

Cu and Ag nanomesh electrodes with a thickness of ~3µm have an enhanced surface area of ~40 - 50x compared to planar electrodes (see SI) which enables significant lower potentials at the same applied current density per geometric area (450mV and 250mV lower on Cu and Ag nanomeshes, respectively) as shown in Figure 2 and 3.

The hydrogen evolution reaction (HER) at our blanket copper substrates is prevalent at all potentials with at least 50% or higher, especially at higher current densities where now active CO_2 depletion is countering the CO_2RR even further. As the HER overpotential is lower than that for CO_2RR,[1,19,24] this catalytic preference is magnified by the enhanced surface area of the nanomesh resulting in a shift of -450mV. This strong reduction in overpotential for CO_2RR combined with the more severe active CO_2 depletion explains the very small formation of CO_2 products. The fact that only ethylene is formed, and no methane supports that the potential has moved outside the potential window for methane, which indeed requires typically a slightly

higher overpotential.[1] The HER current is distributed over the available surface area, lowering the overpotential for HER similar as what was found for Ni nanomesh.[17] Considering this, avoiding the HER that decreases the faradaic efficiency to valuable CO_2RR products on high surface area Cu electrodes in aqueous cells is a challenging task and can only go along with proper CO_2 availability throughout the 3D-nanoarchitecture together with catalytic surface properties that promote the formation of the desired CO_2RR product.

On Ag electrodes CO* is adsorbed weakly and CO is easily released as CO_2RR product as seen by the high amount of CO formed already on planar Ag electrodes in **Figure 3**.[24] At the same time H* adsorbs much weaker on Ag than on Cu and the selective formation of CO from CO_2 occurs on Ag at lower overpotentials than the competing HER.[19,24] Thus, the more catalytically active CO_2RR to CO is in this case magnified by the area enhancement of the Ag nanomesh resulting in a shift to less negative potentials by ~250mV (see **Figure 3**). The faradaic efficiency for HER to CO_2RR is found to be similar for planar and nanomesh electrodes. As compared to planar electrodes more active CO_2 depletion could be expected due to the diffusion of OH^- formed by the HER and CO_2RR out of the nanomesh, the catalytic preference over hydrogen dominates at these lower overpotentials. Hence, the shift in overpotential leads to an improved energy efficiency for the same throughput and faradaic efficiency. Moreover, the lower overpotentials also made the CO_2RR more selective towards CO.

Finally, the effect of pH gradient throughout the nanomesh can affect the CO_2RR on Cu and Ag electrodes. For Cu electrodes, several of the CO_2 reaction pathways are considered pH dependent. As an example, the overpotential for the C−C coupling of CO, which is considered as a key step in the formation of C_2H_4, is known to depend on the surface pH.[25,28,29] Figure 5(b) showed that the surface pH depends strongly on the applied current density and increases

significantly compared to the bulk electrolyte. Hence, the potential (current) dependent product selectivity can be indirectly the result of changing surface pH. As such, the pH gradient inside nanomesh is likely to affect product selectivity at different locations along the nanomesh thickness. Even though we cannot exclude such effects for copper, we believe that the active CO_2 depletion will be the dominant factor with increasing pH. For Ag catalysts it was shown that there is typically no significant impact on the catalytic pathway of CO from CO_2 originating from pH variations.[38]

5. Conclusions

To conclude, high surface area metal electrodes are a very attractive option for CO_2RR, however we show that the extended surface area of our nanomesh electrodes primarily enhance the catalytic reaction with the lowest overpotential. Since our electrodeposited copper is kinetically more active towards HER the high surface area of the nanomesh promotes the formation of H_2 accompanied by a pronounced potential shift to less negative potentials outside the required overpotential window for CO_2RR products. In contrast, silver nanomesh electrodes with the same nano-architecture are more catalytic active towards the CO_2RR to CO compared to HER and indeed the CO_2RR is enhanced by the high surface area. Even though the CO_2 solubility is limited in aqueous electrolytes and active CO_2 depletion by solution alkalinization and the (bi)carbonate equilibrium is detrimental to the CO_2 availability at the electrode surface, for Ag nanomesh compared to planar electrodes the energy efficiency is increased by lowering the overpotential for CO formation by 250mV. To improve the throughput, the low CO_2 solubility can be overcome by increasing the partial pressure of CO_2 above 1 bar or by CO_2 supply directly from the gas phase. Note that also in state-of-the-art gas diffusion electrodes or GDE active CO_2

depletion will play an important role in reducing the CO_2 availability at the catalyst. Indeed, the commonly employed few hundred μm thick carbon-based catalyst substrate becomes quickly flooded with electrolyte upon longer operation, which will contribute to the active removal of CO_2 in the porous substrate. [39,40]. Upon GDE flooding typically a switch in selectivity is observed towards the hydrogen evolution reaction (HER) similar to what is shown in this work. The causes of electrode flooding are related to the increased wetting of the initially hydrophobic gas diffusion layer, which was found to be introduced by the strong negative potential required to drive the CO2 reduction. [40] We have shown that the high surface area Ag nanomesh electrodes can decrease the overpotential towards the CO_2RR and therefore may also decrease the risk of electrode flooding. Novel electrode designs without the need of thick carbon-based gas diffusion layers would minimize the effect of flooding of the latter, however, currently it functions also as an electronic back-contact due to the poor conductivity of the GDE catalyst layer. The rigid metal nanomesh structure is a good electronic conductor and does not need back contacting. Having a thin nanostructured metal electrode like the nanomesh could then offer more robust long-term GDE operation as compared to state-of-the-art.

Figures

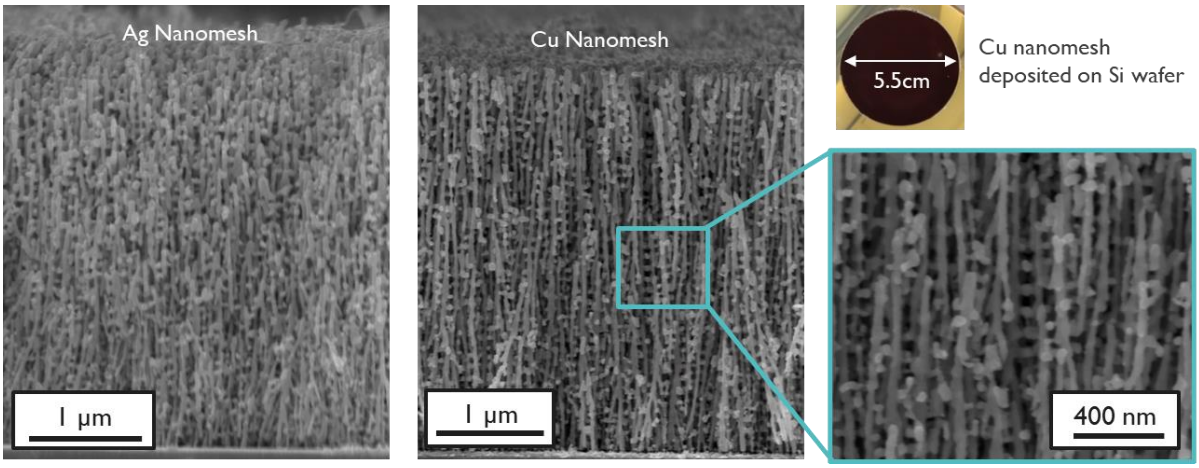

Figure 1: SEM images of Ag and Cu nanomesh electrodes on wafer substrates

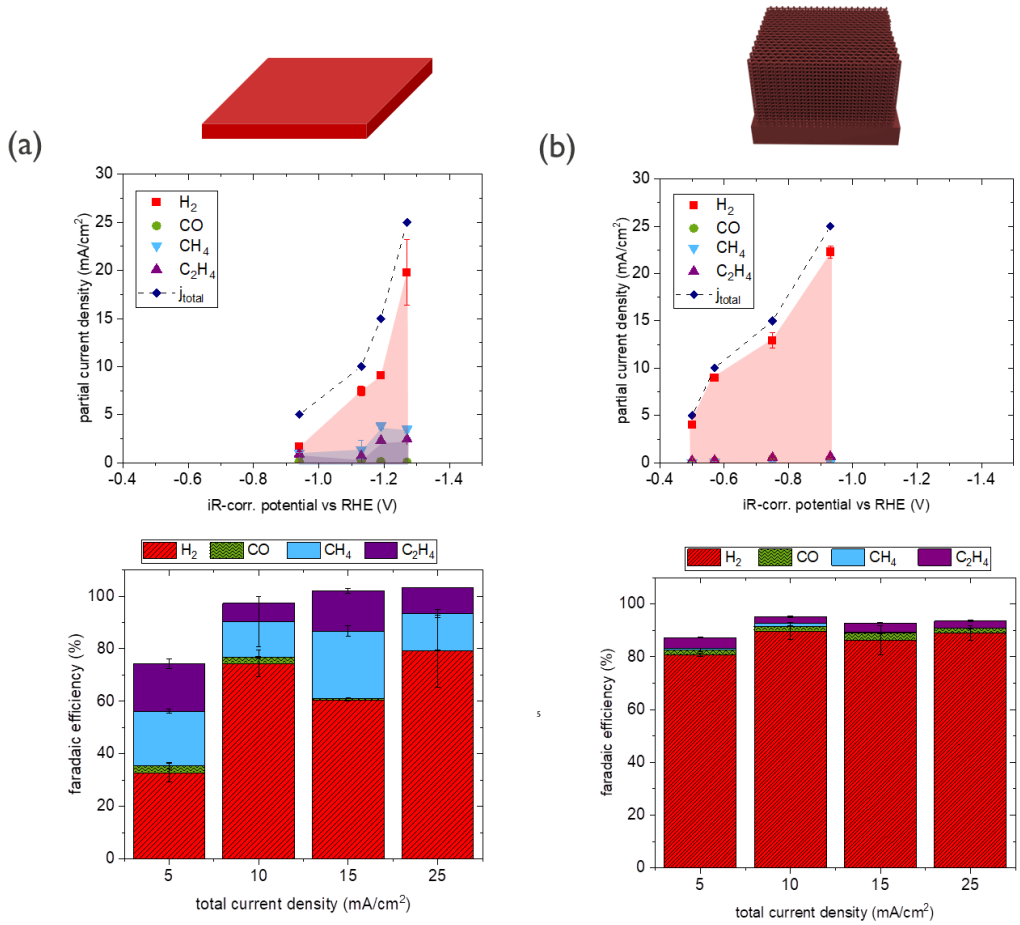

Figure 2: Partial current densities and faradaic efficiencies towards gaseous CO_2RR products and H_2 at constant current densities 5-25mA/cm$^2_{geo}$ using (a) planar Cu, (b) Cu nanomesh as electrodes

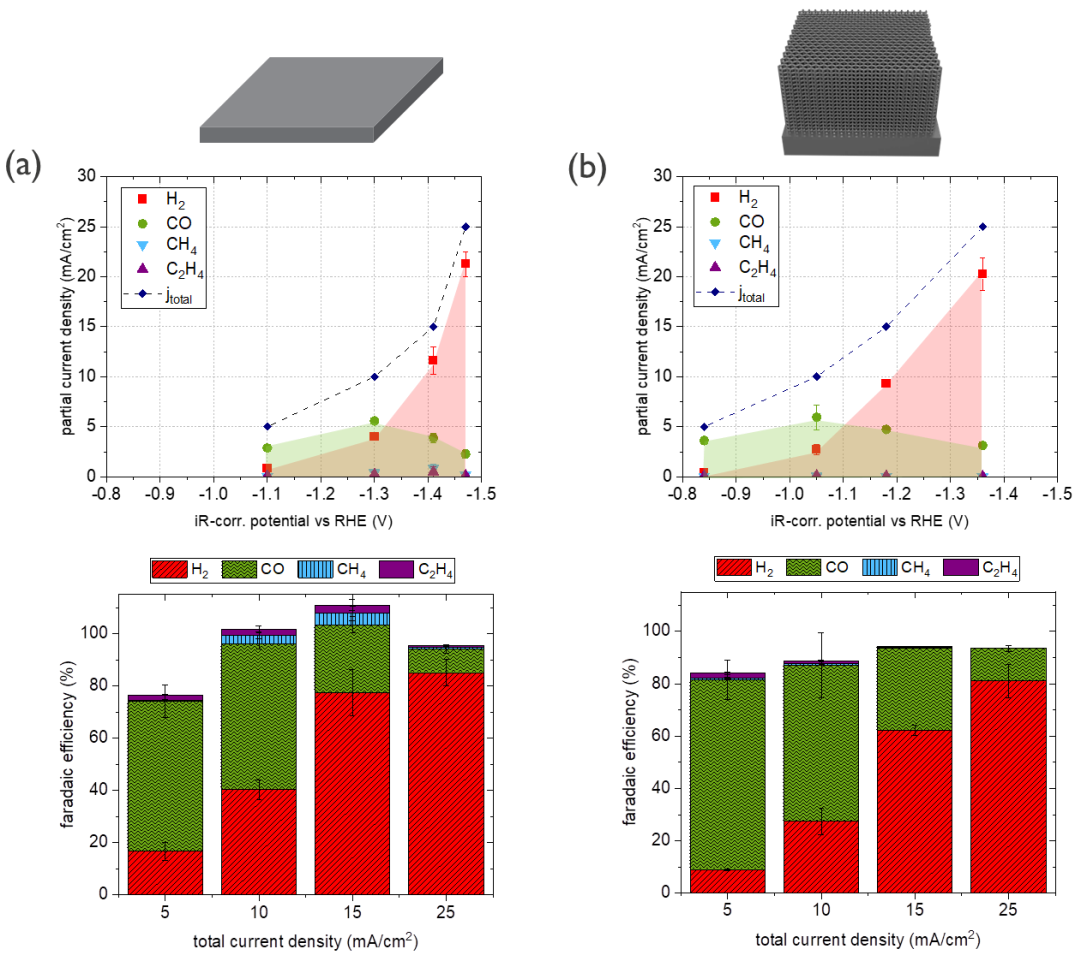

Figure 3: Partial current densities and faradaic efficiencies towards gaseous CO_2RR products and H_2 at constant current densities 5-25mA/cm$^2_{geo}$ using (a) planar Ag, (b) Ag nanomesh as electrodes

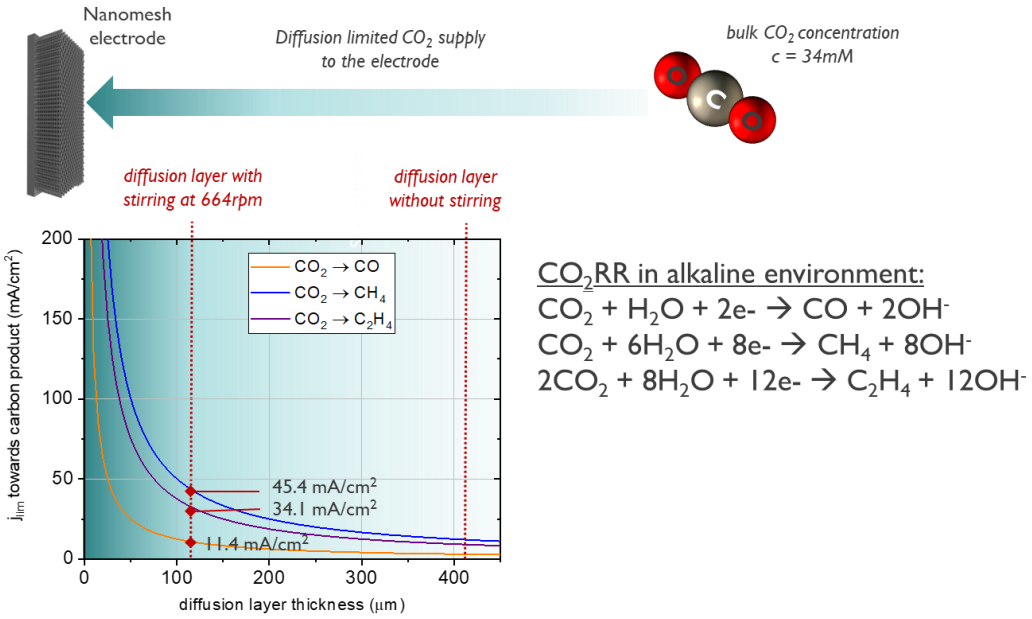

Figure 4: Limiting current density to CO_2RR products by considering the incoming CO_2 flux in dependence of the diffusion layer thickness with the indicated 110µm and 410 µm thick diffusion layer with/without stirring as determined for the cell used within this work

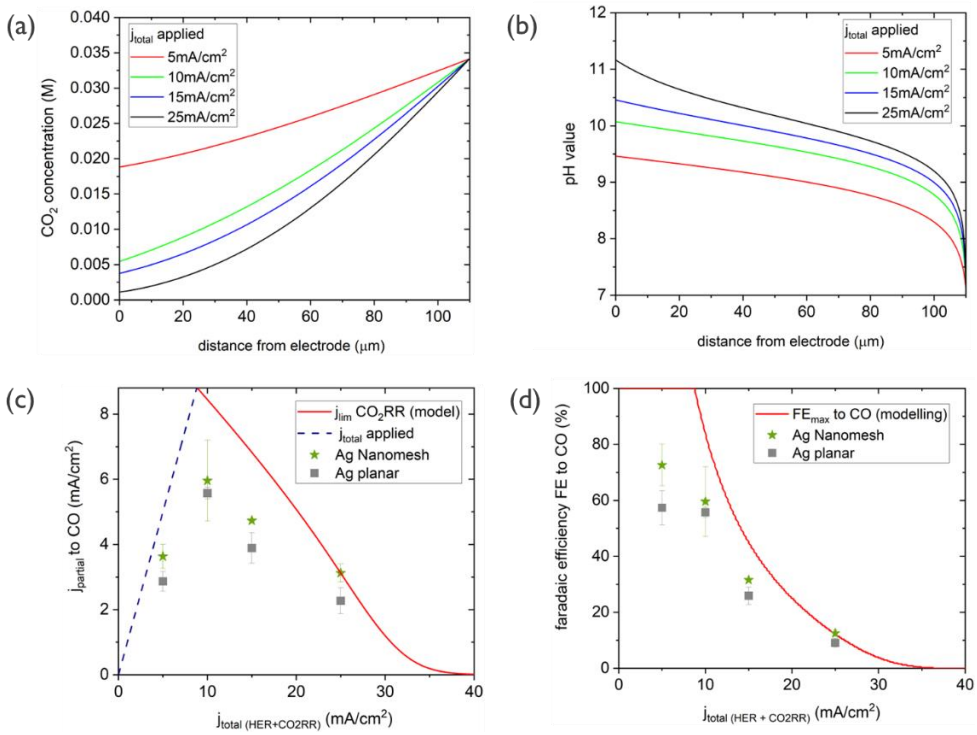

Figure 5: Plots obtained from steady-state diffusion model including the CO:H_2 ratio from planar Ag (a) CO_2 concentration profile in the diffusion layer δ (110μm) and at the electrode surface at different applied current densities, (b) pH profiles in the δ and at the electrode surface at different applied current densities (c) limiting partial current density to CO ($j_{partial}$) from the modelling the active CO_2 depletion and experimental results on planar Ag and nanomesh electrodes, (d) maximum faradaic efficiency to CO in dependence of the applied current densities compared to experimental results on planar Ag and nanomesh electrodes

Declaration of Competing Interest

The authors declare that they have no known competing financial interests or personal relationships that could have appeared to influence the work reported in this paper.

Credit authorship contribution statement

Nina Plankensteiner: conceptualization, methodology, validation, investigation, data interpretation, writing – original draft, writing – review & editing, funding acquisition. **Noah Rondou**: methodology, validation, investigation, data interpretation, writing – review & editing. **Martijn J.W. Blom**: formal analysis, validation, data interpretation, writing – review & editing. **Anna Staerz**: resources, investigation, writing – review & editing. **Cole Smith**: resources, investigation. **Maarten Mees:** data interpretation, resources, funding acquisition. **Philippe M. Vereecken**: conceptualization, methodology, data interpretation, supervision, writing – review & editing, funding acquisition.

Acknowledgements

This work was funded by the European Union's Horizon 2020 research and innovation programme under the Marie Skłodowska-Curie Individual Fellowship grant agreement No 101032191. The authors acknowledge Anupam Tripathy for providing some of the copper nanomeshes used within this work.

Supplementary materials

Includes characterization of the Ag and Cu planar and nanomesh electrode, experimental details and data for the CO_2RR in the liquid H-cell and the equations used for the computational modelling of CO_2 mass transport.

References

[1] Y. Hori, Electrochemical CO2 Reduction on Metal Electrodes, Modern Aspects of Electrochemistry. (2008) 89–189. https://doi.org/10.1007/978-0-387-49489-0_3.

[2] I.E.L. Stephens, K. Chan, A. Bagger, S.W. Boettcher, J. Bonin, E. Boutin, A.K. Buckley, R. Buonsanti, E.R. Cave, X. Chang, S.W. Chee, A.H.M. da Silva, P. de Luna, O. Einsle, B. Endrődi, M. Escudero-Escribano, J. V. Ferreira de Araujo, M.C. Figueiredo, C. Hahn, K.U. Hansen, S. Haussener, S. Hunegnaw, Z. Huo, Y.J. Hwang, C. Janáky, B.S. Jayathilake, F. Jiao, Z.P. Jovanov, P. Karimi, M.T.M. Koper, K.P. Kuhl, W.H. Lee, Z. Liang, X. Liu, S. Ma, M. Ma, H.S. Oh, M. Robert, B.R. Cuenya, J. Rossmeisl, C. Roy, M.P. Ryan, E.H. Sargent, P. Sebastián-Pascual, B. Seger, L. Steier, P. Strasser, A.S. Varela, R.E. Vos, X. Wang, B. Xu, H. Yadegari, Y. Zhou, 2022 roadmap on low temperature electrochemical CO2 reduction, Journal of Physics: Energy. 4 (2022) 042003. https://doi.org/10.1088/2515-7655/AC7823.

[3] Q. Lu, J. Rosen, F. Jiao, Nanostructured metallic electrocatalysts for carbon dioxide reduction, ChemCatChem. 7 (2015) 38–47. https://doi.org/10.1002/CCTC.201402669.

[4] S. Nitopi, E. Bertheussen, S.B. Scott, X. Liu, A.K. Engstfeld, S. Horch, B. Seger, I.E.L. Stephens, K. Chan, C. Hahn, J.K. Nørskov, T.F. Jaramillo, I. Chorkendorff, Progress and Perspectives of Electrochemical CO2 Reduction on Copper in Aqueous Electrolyte, Chem Rev. 119 (2019) 7610–7672. https://doi.org/10.1021/acs.chemrev.8b00705.

[5] R. Kas, K. Yang, D. Bohra, R. Kortlever, T. Burdyny, W.A. Smith, Electrochemical CO2 reduction on nanostructured metal electrodes: fact or defect?, Chem Sci. 11 (2020) 1738–1749. https://doi.org/10.1039/C9SC05375A.

[6] C.W. Li, M.W. Kanan, CO 2 reduction at low overpotential on Cu electrodes resulting from the reduction of thick Cu 2O films, J Am Chem Soc. 134 (2012) 7231–7234. https://doi.org/10.1021/JA3010978/SUPPL_FILE/JA3010978_SI_001.PDF.

[7] T.T. Zhuang, Y. Pang, Z.Q. Liang, Z. Wang, Y. Li, C.S. Tan, J. Li, C.T. Dinh, P. De Luna, P.L. Hsieh, T. Burdyny, H.H. Li, M. Liu, Y. Wang, F. Li, A. Proppe, A. Johnston, D.H. Nam, Z.Y. Wu, Y.R. Zheng, A.H. Ip, H. Tan, L.J. Chen, S.H. Yu, S.O. Kelley, D. Sinton, E.H. Sargent, Copper nanocavities confine intermediates for efficient electrosynthesis of C3 alcohol fuels from carbon monoxide, Nature Catalysis 2018 1:12. 1 (2018) 946–951. https://doi.org/10.1038/s41929-018-0168-4.

[8] K.D. Yang, W.R. Ko, J.H. Lee, S.J. Kim, H. Lee, M.H. Lee, K.T. Nam, Morphology-Directed Selective Production of Ethylene or Ethane from CO2 on a Cu Mesopore Electrode, Angewandte Chemie International Edition. 56 (2017) 796–800. https://doi.org/10.1002/ANIE.201610432.

[9] A. Loiudice, P. Lobaccaro, E.A. Kamali, T. Thao, B.H. Huang, J.W. Ager, R. Buonsanti, Tailoring Copper Nanocrystals towards C2 Products in Electrochemical CO2 Reduction, Angewandte Chemie International Edition. 55 (2016) 5789–5792. https://doi.org/10.1002/ANIE.201601582.

[10] G. Mangione, J. Huang, R. Buonsanti, C. Corminboeuf, Dual-facet mechanism in copper nanocubes for electrochemical CO2 Reduction into Ethylene, Journal of Physical Chemistry Letters. 10 (2019) 4259–4265. https://doi.org/10.1021/ACS.JPCLETT.9B01471/SUPPL_FILE/JZ9B01471_SI_001.PDF.

[11] Y. Hori, H. Konishi, T. Futamura, A. Murata, O. Koga, H. Sakurai, K. Oguma, “Deactivation of copper electrode” in electrochemical reduction of CO2, Electrochim Acta. 50 (2005) 5354–5369. https://doi.org/10.1016/J.ELECTACTA.2005.03.015.

[12] A. Wuttig, Y. Surendranath, Impurity Ion Complexation Enhances Carbon Dioxide Reduction Catalysis, ACS Catal. 5 (2015) 4479–4484. https://doi.org/10.1021/ACSCATAL.5B00808/SUPPL_FILE/CS5B00808_SI_001.PDF.

[13] T. Burdyny, W.A. Smith, CO2 reduction on gas-diffusion electrodes and why catalytic performance must be assessed at commercially-relevant conditions, Energy Environ Sci. 12 (2019) 1442–1453. https://doi.org/10.1039/C8EE03134G.

[14] J.J. Carroll, J.D. Slupsky, A.E. Mather, The Solubility of Carbon Dioxide in Water at Low Pressure, J Phys Chem Ref Data. 20 (1991) 1201–1209. https://doi.org/10.1063/1.555900.

[15] W.M.Haynes, CRC Handbook of Chemistry and Physics, 95th ed., Taylor & Francis Group, 2014. https://edisciplinas.usp.br/pluginfile.php/4557662/mod_resource/content/1/CRC%20Handbook%20of%20Chemistry%20and%20Physics%2095th%20Edition.pdf (accessed April 28, 2023).

[16] E.L. Clark, J. Resasco, A. Landers, J. Lin, L.T. Chung, A. Walton, C. Hahn, T.F. Jaramillo, A.T. Bell, Standards and Protocols for Data Acquisition and Reporting for Studies of the Electrochemical Reduction of Carbon Dioxide, ACS Catal. 8 (2018) 6560–6570. https://doi.org/10.1021/ACSCATAL.8B01340/SUPPL_FILE/CS8B01340_SI_001.PDF.

[17] N. Plankensteiner, R. Rupp, P. Steegstra, S. Singh, J.G. Canto, S. Wodarz, M.J.W. Blom, J. John, M. Mees, P.M. Vereecken, Freestanding μm-thin nanomesh electrodes exceeding 100x current density enhancement for high-throughput electrochemical applications, Mater Today Energy. (2022) 101172. https://doi.org/10.1016/J.MTENER.2022.101172.

[18] S.P. Zankowski, P.M. Vereecken, Combining High Porosity with High Surface Area in Flexible Interconnected Nanowire Meshes for Hydrogen Generation and beyond, ACS Appl Mater Interfaces. 10 (2018) 44634–44644. https://doi.org/10.1021/acsami.8b15888.

[19] J. Greeley, T.F. Jaramillo, J. Bonde, I. Chorkendorff, J.K. Nørskov, Computational high-throughput screening of electrocatalytic materials for hydrogen evolution, Nature Materials 2006 5:11. 5 (2006) 909–913. https://doi.org/10.1038/nmat1752.

[20] Y.J. Zhang, V. Sethuraman, R. Michalsky, A.A. Peterson, Competition between CO2 reduction and H2 evolution on transition-metal electrocatalysts, ACS Catal. 4 (2014) 3742–3748. https://doi.org/10.1021/CS5012298/SUPPL_FILE/CS5012298_SI_001.PDF.

[21] S. Hernández, M.A. Farkhondehfal, F. Sastre, M. Makkee, G. Saracco, N. Russo, Syngas production from electrochemical reduction of CO2: current status and prospective implementation, Green Chemistry. 19 (2017) 2326–2346. https://doi.org/10.1039/C7GC00398F.

[22] T. Zheng, K. Jiang, H. Wang, Recent Advances in Electrochemical CO2-to-CO Conversion on Heterogeneous Catalysts, Advanced Materials. 30 (2018) 1802066. https://doi.org/10.1002/ADMA.201802066.

[23] K.P. Kuhl, T. Hatsukade, E.R. Cave, D.N. Abram, J. Kibsgaard, T.F. Jaramillo, Electrocatalytic conversion of carbon dioxide to methane and methanol on transition metal surfaces, J Am Chem Soc. 136 (2014) 14107–14113. https://doi.org/10.1021/JA505791R/SUPPL_FILE/JA505791R_SI_001.PDF.

[24] A. Bagger, W. Ju, A.S. Varela, P. Strasser, J. Rossmeisl, Electrochemical CO2 Reduction: A Classification Problem, ChemPhysChem. 18 (2017) 3266–3273. https://doi.org/10.1002/CPHC.201700736.

[25] T.K. Todorova, M.W. Schreiber, M. Fontecave, Mechanistic Understanding of CO2 Reduction Reaction (CO2RR) Toward Multicarbon Products by Heterogeneous Copper-Based Catalysts, ACS Catal. 10 (2020) 1754–1768. https://doi.org/10.1021/ACSCATAL.9B04746/ASSET/IMAGES/MEDIUM/CS9B04746_0010.GIF.

[26] P. Lobaccaro, M.R. Singh, E.L. Clark, Y. Kwon, A.T. Bell, J.W. Ager, Effects of temperature and gas–liquid mass transfer on the operation of small electrochemical cells for the quantitative evaluation of CO2 reduction electrocatalysts, Physical Chemistry Chemical Physics. 18 (2016) 26777–26785. https://doi.org/10.1039/C6CP05287H.

[27] N. Gupta, M. Gattrell, B. MacDougall, Calculation for the cathode surface concentrations in the electrochemical reduction of CO2 in KHCO3 solutions, J Appl Electrochem. 36 (2006) 161–172. https://doi.org/10.1007/S10800-005-9058-Y/METRICS.

[28] K.J.P. Schouten, Z. Qin, E.P. Gallent, M.T.M. Koper, Two pathways for the formation of ethylene in CO reduction on single-crystal copper electrodes, J Am Chem Soc. 134 (2012) 9864–9867. https://doi.org/10.1021/JA302668N/SUPPL_FILE/JA302668N_SI_001.PDF.

[29] F.S. Roberts, K.P. Kuhl, A. Nilsson, Electroreduction of Carbon Monoxide Over a Copper Nanocube Catalyst: Surface Structure and pH Dependence on Selectivity, ChemCatChem. 8 (2016) 1119–1124. https://doi.org/10.1002/CCTC.201501189.

[30] D. Chu, S. Gilman, The Influence of Methanol on O 2 Electroreduction at a Rotating Pt Disk Electrode in Acid Electrolyte, J Electrochem Soc. 141 (1994) 1770–1773. https://doi.org/10.1149/1.2055002/XML.

[31] S. Gottesfeld, I.D. Raistrick, S. Srinivasan, Oxygen Reduction Kinetics on a Platinum RDE Coated with a Recast Nafion Film, J Electrochem Soc. 134 (1987) 1455–1462. https://doi.org/10.1149/1.2100689/XML.

[32] S. Zhao, R. Jin, R. Jin, Opportunities and Challenges in CO2 Reduction by Gold- and Silver-Based Electrocatalysts: From Bulk Metals to Nanoparticles and Atomically Precise Nanoclusters, ACS Energy Lett. 3 (2018) 452–462. https://doi.org/10.1021/acsenergylett.7b01104.

[33] Y. Lum, B. Yue, P. Lobaccaro, A.T. Bell, J.W. Ager, Optimizing C-C Coupling on Oxide-Derived Copper Catalysts for Electrochemical CO2 Reduction, Journal of Physical Chemistry C. 121 (2017) 14191–14203. https://doi.org/10.1021/ACS.JPCC.7B03673/SUPPL_FILE/JP7B03673_SI_001.PDF.

[34] R. Kas, R. Kortlever, H. Yılmaz, M.T. M Koper, G. Mul, R. Kas, G. Mul, R. Kortlever, M.T. M Koper, H. Yılmaz, Manipulating the Hydrocarbon Selectivity of Copper Nanoparticles in CO 2 Electroreduction by Process Conditions, ChemElectroChem. 2 (2015) 354–358. https://doi.org/10.1002/celc.201402373.

[35] D. Raciti, K.J. Livi, C. Wang, Highly Dense Cu Nanowires for Low-Overpotential CO 2 Reduction, Nano Lett. 15 (2015) 6829–6835. https://doi.org/10.1021/ACS.NANOLETT.5B03298/SUPPL_FILE/NL5B03298_SI_001.PDF.

[36] A. Dutta, M. Rahaman, N.C. Luedi, M. Mohos, P. Broekmann, Morphology Matters: Tuning the Product Distribution of CO2 Electroreduction on Oxide-Derived Cu Foam Catalysts, ACS Catal. 6 (2016) 3804–3814. https://doi.org/10.1021/ACSCATAL.6B00770/SUPPL_FILE/CS6B00770_SI_001.PDF.

[37] S. Sen, D. Liu, G.T.R. Palmore, Electrochemical reduction of CO2 at copper nanofoams, ACS Catal. 4 (2014) 3091–3095. https://doi.org/10.1021/CS500522G/SUPPL_FILE/CS500522G_SI_001.PDF.

[38] M.R. Singh, J.D. Goodpaster, A.Z. Weber, M. Head-Gordon, A.T. Bell, Mechanistic insights into electrochemical reduction of CO2 over Ag using density functional theory and transport models, Proc Natl Acad Sci U S A. 114 (2017) E8812–E8821. https://doi.org/10.1073/PNAS.1713164114/SUPPL_FILE/PNAS.1713164114.SAPP.PDF.

[39] A.A. Samu, I. Szenti, Á. Kukovecz, B. Endrődi, C. Janáky, Systematic screening of gas diffusion layers for high performance CO2 electrolysis, Communications Chemistry 2023 6:1. 6 (2023) 1–9. https://doi.org/10.1038/s42004-023-00836-2.

[40] K. Yang, R. Kas, W.A. Smith, T. Burdyny, Role of the Carbon-Based Gas Diffusion Layer on Flooding in a Gas Diffusion Electrode Cell for Electrochemical CO2Reduction, ACS Energy Lett. 6 (2021) 33–40. https://doi.org/10.1021/ACSENERGYLETT.0C02184/ASSET/IMAGES/LARGE/NZ0C02184_0004.JPEG.